Performance Analysis of Electromechanical Flywheel for Electric Vehicles Based on Planetary Gear Mechanism

Pengwei Wang, Tianqi Gu, Binbin Sun, Rui Dang, Zhenwei Wang and Weichong Li

Abstract—**As a new auxiliary energy power unit, electromechanical flywheel device based on planetary gear mechanism directly influences the power performance and economy performance of electric vehicles. The reliability, safety and economy of electromechanical flywheel device are affected by its own dynamics, mechanics, efficiency and other performance characteristics. Therefore, based on the developed planetary gear mechanism, the electromechanical flywheel device is studied in this paper. Firstly, the device topology, operating mode and other characteristics are analyzed, and the device dynamics model is established. Then, the mathematical model of high-speed flywheel stress analysis is established, and the high-speed flywheel stress and modal characteristics are analyzed. Furthermore, the loss model of the device is established, and the efficiency characteristics of the device under different states of energy (SOE) are analyzed. Finally, the influence of electromechanical flywheel device on vehicle dynamic performance and economic performance is analyzed. Compared with the original single-motor drive scheme, power performance and economical performance have both been improved.**

Index Terms—**electromechanical flywheel, electric vehicle, system dynamics, economy**

I. Introduction

Improving the on-board energy utilization efficiency of electric vehicles and improving the driving range are important goals of the electric vehicle industry [1]. Due to the constraints of the system topology, the single battery scheme could only realize electric vehicles efficient operation under partial steady-state operating conditions [2]. With the development of electric-electric composite energy system, the working conditions for efficient operation of electric vehicles are improved [3]. Flywheel energy storage device has the advantages of high energy conversion efficiency and high power density. It can effectively improve the energy utilization efficiency of electric vehicles as an auxiliary energy system [4-6].

As shown in Fig. 1, the existing flywheel energy storage devices can be classified into two types according to energy input and output: electrical energy storage and mechanical energy storage [7]. The electric energy storage type could be used for power system regulation and satellite attitude control. Energy storage and energy consumption performance are the key parameters to measure the performance of flywheel energy storage device. The performance can be improved by designing and controlling super-high-speed and high-efficiency flywheel, which involves technical problems such as composite materials, magnetic bearings and vacuum chambers and high costs [8]. The above problems limit the application of electric energy storage flywheel system in electric vehicles.

The existing mechanical flywheel energy storage system usually transfers the flywheel energy directly through the continuously variable transmission (CVT), which does not involve the energy conversion link. This scheme has high system efficiency, compact structure and good energy saving effect [9-10]. However, due to the limitation of the CVT speed ratio adjustment range, the flywheel energy storage system still has the problem that the flywheel energy can not be deeply released and feedback.

The electromechanical flywheel device based on planetary gear mechanism mainly adopts the conventional mechanical bearing and non-vacuum design scheme, which can significantly reduce the device cost. Through the planetary gear mechanism, the speed regulating motor can be controlled according to the characteristics of vehicle working conditions to solve the problem of flywheel energy deep release and feedback [11]. However, as a new flywheel energy storage device, its dynamics, mechanics, efficiency and other characteristics are still unclear. Therefore, based on the developed planetary gear mechanism, the electromechanical flywheel device is studied in this paper. Firstly, the device topology, operating mode and other characteristics are analyzed, and the device dynamics model

Manuscript received May 26, 2022; revised October 10, 2022.

This work was supported in part by the Innovation team project of "Qing-Chuang science and technology plan" of colleges and universities in Shandong Province 2021KJ083, the Major Innovation Projects in Shandong under Grant 2020CXGC010405 and 2020CXGC010406, the National Natural Science Foundation Project of China under Grant 51805301 and 52102465, the Postdoctoral Science Foundation of China and Shandong under Grant 2020M680091 and 202003042.

Pengwei Wang is a Professor of School of Transportation and Vehicle Engineering, Shandong University of Technology, Zibo, 255000 PR China. (e-mail: wpwk16@163.com).

Tianqi Gu is a graduate student of School of Transportation and Vehicle Engineering, Shandong University of Technology, Zibo, 255000 PR China. (e-mail: tianqi.gu@outlook.com).

Binbin Sun is a Professor of School of Transportation and Vehicle Engineering, Shandong University of Technology, Zibo, 255000 PR China. (corresponding author to provide phone: 86-13708941464; e-mail: sunbin_sdut@126.com).

Rui Dang is a graduate student of School of Transportation and Vehicle Engineering, Shandong University of Technology, Zibo, 255000 PR China. (e-mail: 18953820262@163.com).

Zhenwei Wang is a graduate student of School of Transportation and Vehicle Engineering, Shandong University of Technology, Zibo, 255000 PR China. (e-mail: zhenweiwang2022@163.com).

Weichong Li is a graduate student of School of Transportation and Vehicle Engineering, Shandong University of Technology, Zibo, 255000 PR China. (e-mail: l17616530216@163.com).

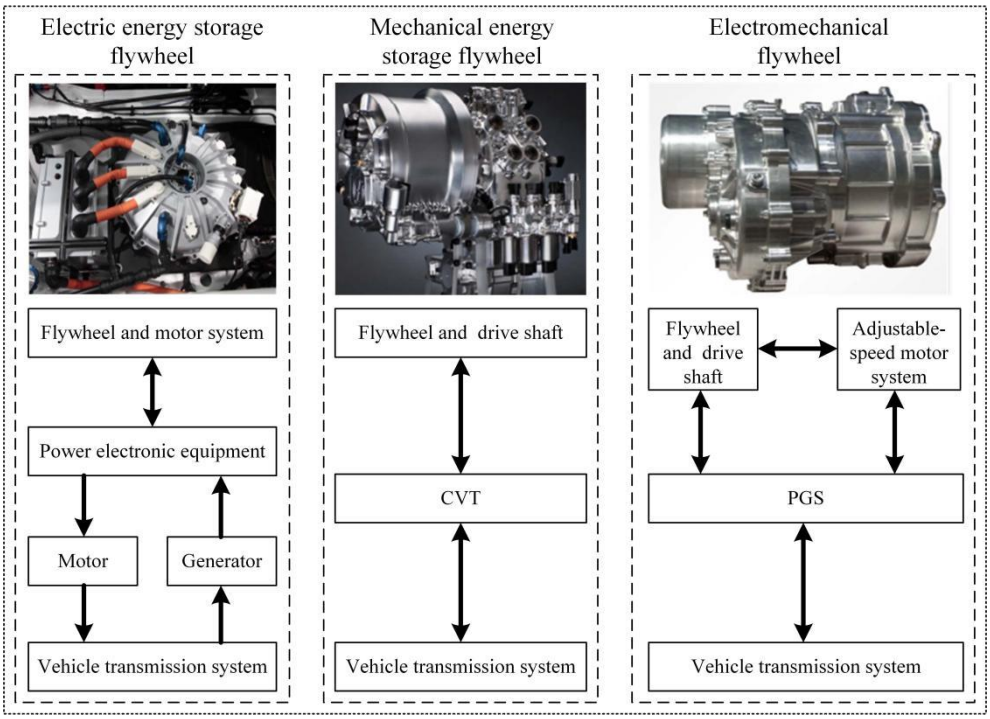

Fig. 1 Structure and energy flow of different flywheel systems

is established. Then, the mathematical model of high-speed flywheel stress analysis is established, and the high-speed flywheel stress and modal characteristics are analyzed. Furthermore, the loss model of the device is established, and the efficiency characteristics of the device under different states of energy (SOE)are analyzed. Finally, the influence of electromechanical flywheel device on vehicle dynamic performance and economic performance is analyzed.

II. Electromechanical Flywheel Dynamics Characterization and Mathematical Modeling

A. Topology scheme analysis

As is shown in Fig. 2, the electromechanical flywheel device consists of flywheel, planetary gear mechanism, speed control motor, and one-way locking mechanism. The one-way locking mechanism is connected with the flywheel, which ensure the flywheel rotates at positive speed and locks when it rotates in reverse direction. The flywheel is connected to the ring gear of the planetary gear mechanism through the reduction gear, the motor output shaft is connected to the sun gear through the spline, and the planet carrier is connected to the output shaft for external power output.

The following speed relationship exists between the sun gear, ring gear and planet carrier.

$$n_c = \frac{1}{1+k} n_s + \frac{k}{1+k} n_r \tag{1}$$

Where, n_s,n_r,n_c are the rotate speed of the sun gear, ring gear and planet carrier, respectively. k is the characteristic parameter of the planet row. It is the ratio between the number of teeth in the ring gear and that of the sun gear.

As the energy loss in stable operation is negligible, the following torque relationship exists between the sun gear, ring gear and planet carrier.

$$T_c = -(1+k)T_s = -[(1+k)/k]T_r \tag{2}$$

Where, T_s, T_r, T_c are the rotational speeds of the sun gear, ring gear and planet carrier, respectively.

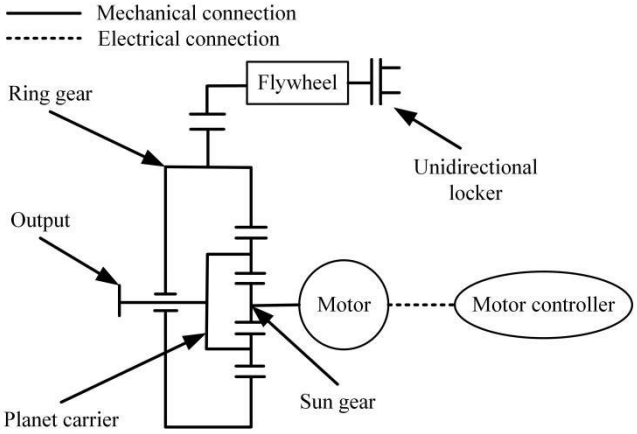

Fig. 2 Topology scheme of electromechanical flywheel device

B. Device operating modes analysis and dynamics modeling

(1) When the vehicle starts for the first time, the flywheel speed is zero, and the flywheel is locked, the speed control motor starts positive rotation and outputs positive torque T_{srm}, which is amplified k+1 times by the planetary gear mechanism and loaded to the output shaft, so the starting torque increases and the acceleration time decreases. The torque relationship of the wheel at start is as follows.

$$T_{dw} = -(k+1) i_{c\text{-}dw} T_{srm} \tag{3}$$

Where, T_{dw}, T_{srm} are the wheel torque and the speed control motor torque, respectively. k is the characteristic parameter of the planet row. $i_{c\text{-}dw}$ is the transmission ratio from planet carrier to wheel.

(2) When the vehicle accelerates, the speed control motor is still positive rotating and outputting positive torque T_{srm}, which is amplified k+1 times by the planetary gear mechanism and loaded to the output shaft, and the wheel torque increases.

$$T_{dw} = -(k+1)i_{c\text{-}dw}T_{srm} \tag{4}$$

At the same time, the torque T_{srm} acts on the flywheel through the planetary mechanism, which reduces the flywheel speed.

$$T_{fw} = \frac{k}{i_{fw\text{-}r}}T_{srm} \tag{5}$$

Where, T_{fw} is the torque of flywheel, $i_{fw\text{-}r}$ is the transmission ratio from flywheel to ring gear.

(3) In the process of vehicle deceleration (deceleration a mode), when the braking energy is high, the energy recovery rate of speed control motor alone is slow. Then releasing the flywheel brake, the speed control motor starts to output negative torque T_{srm}, its speed decreases and switches to the power generation state. The torque T_{srm} is amplified by the planetary gear mechanism and acts on the output shaft to reduce the vehicle speed.

$$T_{dw} = -(k+1)i_{c\text{-}dw}T_{srm} \tag{6}$$

Meanwhile, the torque T_{srm} acts on the flywheel through the planetary mechanism to increase the flywheel speed.

$$T_{fw} = \frac{k}{i_{fw\text{-}r}}T_{srm} \tag{7}$$

In this mode, the speed relationship between flywheel, speed control motor and wheel is as follows.

$$n_{dw} = \frac{1}{i_{c\text{-}dw}}\left(\frac{1}{1+k}n_{srm} + \frac{k}{1+k}\frac{n_{fw}}{i_{fw\text{-}r}}\right) \tag{8}$$

Where, n_{dw}, n_{srm} and n_{fw} are the rotational speed of wheel, speed control motor and flywheel, respectively.

(4) In the process of vehicle deceleration (deceleration b mode), the braking energy is generated slowly and the flywheel takes longer to recharge. In the meantime, the speed control motor starts to output negative torque T_{srm} and the speed is accelerated in the reverse direction, working in the electric state. The torque T_{srm} is amplified by the planetary gear mechanism and acts on the output shaft to reduce the wheel speed. The torque relationship of the wheel is as follows.

$$T_{dw} = -(k+1)i_{c\text{-}dw}T_{srm} \tag{9}$$

Meantime, the torque T_{srm} acts on the flywheel through the planetary gear mechanism and the flywheel speed increases until the vehicle decelerates and stops.

$$T_{fw} = \frac{k}{i_{fw\text{-}r}}T_{srm} \tag{10}$$

(5) The vehicle decelerates until parking and the remaining kinetic energy of the flywheel needs to be recovered before stalling. The speed control motor starts to output negative torque T_{srm} and the speed is accelerated in the reverse direction, working in the generator mode. At the same time this torque is applied to the flywheel by the planetary mechanism, which decelerates the flywheel to stop.

The speed and torque relationship between the flywheel and the speed control motor are as follows, respectively.

$$n_{srm} = -\frac{k}{i_{fw\text{-}r}}n_{fw} \tag{11}$$

$$T_{fw} = \frac{k}{i_{fw\text{-}r}}T_{srm} \tag{12}$$

III. Analysis and Verification of Mechanical Properties of Composite Flywheel

Flywheel is the core component of electromechanical flywheel system, which has a direct impact on the system performance. The flywheel needs to be charged and discharged quickly and frequently, which makes the rotation speed of the flywheel change frequently, and its maximum speed reaches 20000 rpm. When the flywheel rotates at high speed, its structural strength, deformation, resonance and other characteristics need to be analyzed.

A. Mathematical model of stress in composite flywheel

In the winding process of composite flywheel, carbon fiber is wound in a ring shape on the hub of the flywheel, so that the carbon fiber bundle forms a thin ring of composite material in one layer on the metal hub of the flywheel, and together with the hub, it forms a composite flywheel. And due to the presence of tensioning force, which causes the interaction between the thin ring of composite material and the hub of metal material, in the following calculation, because the thin ring of carbon fiber wound on the hub with certain tensioning force will produce certain stress on the thin ring of carbon fiber in other layers inside it, it will be equated into a layer of thin ring of carbon fiber assembled on the core with certain amount of overload. Under the action of the carbon fiber tensioning force F, the average annular stress of the wound composite thin layer and the fiber bundle tensioning force satisfy the following relation formula.

$$\sigma_\theta = \frac{1}{t}\int_{r_i}^{r_{i+1}}\sigma_\theta(r)dr = \frac{FV_f}{A_f} \tag{13}$$

Where, t is the thickness of the composite thin layer, F is the tensioning force of the carbon fiber bundle, and V_f is the volume percentage of the carbon fiber. A_f is the cross-sectional area of the carbon fiber bundle.

The radius of the i-th layer of carbon fibers is as follows.

$$R_{i\max} = R_{i\min} + t = R_0 + i \cdot t \tag{14}$$

Where, $R_{i\min}$ is the inner radius of the i-th layer of carbon fibers, $R_{i\max}$ is the outer radius of the i-th layer of carbon fibers, and t is the thickness of a single layer of carbon fibers.

When the first layer of carbon fiber is wound on the metal hub, due to the tensioning force, the pressure P_{in}^1 is

generated on its metal core, and the metal core simultaneously generates a reaction force P_{out}^{1} on the layer of carbon fiber. So the radial and axial stresses of the winding are as follows respectively.

$$\sigma_{r1}=\frac{P_{\text{in}}^{1}\left(\frac{R_{1\min}}{R_{1\max}}\right)^{\lambda+1}}{1-\left(\frac{R_{1\min}}{R_{1\max}}\right)^{2\lambda}}\left[\left(\frac{r_1}{R_{1\max}}\right)^{\lambda-1}-\left(\frac{r_1}{R_{1\max}}\right)^{-\lambda-1}\right] \tag{15}$$

$$\sigma_{\theta 1}=\frac{\lambda P_{\text{in}}^{1}\left(\frac{R_{1\min}}{R_{1\max}}\right)^{\lambda+1}}{1-\left(\frac{R_{1\min}}{R_{1\max}}\right)^{2\lambda}}\left[\left(\frac{r_1}{R_{1\max}}\right)^{\lambda-1}+\left(\frac{r_1}{R_{1\max}}\right)^{-\lambda-1}\right] \tag{16}$$

Where, σ_r , σ_θ are the radial stress and axial stress of the rim. $\lambda=\sqrt{E_\theta / E_r}$, is the ratio of the annular modulus of elasticity and the radial modulus of elasticity of the composite material. r is between $R_{i\min}$ and $R_{i\max}$.

After calculating the radial and axial stresses in the thin carbon fiber ring of the first layer, the radial displacement at its inner diameter is calculated as follows based on parameters such as the elastic modulus and Poisson's ratio of the material.

$$u_{r1}=\frac{R_n-\delta_1}{E_\theta}\cdot\left(\frac{1+\beta_1^{2\lambda}}{1-\beta_1^{2\lambda}}\cdot\lambda+v_{\theta r}\right)\cdot p_{\text{in}}^{1} \tag{17}$$

Where, u_r is the radial displacement of the thin carbon fiber layer; δ is the excess of tension winding equivalent; E_θ is the annular modulus of elasticity; $\beta=(R_n-\delta)/(R_n-\delta+t)$, is the ratio of inner and outer radius; $v_{\theta r}$ is the Poisson's ratio.

From the deformation geometry conditions at the mating interface, we obtain :

$$P_{\text{in}}^{1}=\frac{\delta_1}{\frac{R_n(1-v)}{E}+\frac{R_n-\delta_1}{E_\theta}\left(\frac{1+\beta_1^{2\lambda}}{1-\beta_1^{2\lambda}}\cdot\lambda+v_{\theta r}\right)} \tag{18}$$

Then the outer diameter of the thin ring of the first layer of carbon fiber is obtained as follows.

$$R_{1\max}=(R_n-\delta_1+t)+\frac{R_n-\delta_1+t}{E_\theta}\cdot\frac{2\beta_1^{\lambda+1}}{1-\beta_1^{2\lambda}}\cdot\lambda\cdot p_{\text{in}}^{1} \tag{19}$$

The carbon fiber rotor of the composite flywheel is wound up to the k-th ($1<k<n$) layer, and the thin ring of the metal's core and the $k-1$-th layer of carbon fiber are regarded as the composite core with initial stress 0. The thin ring of the k-th layer and the composite core are regarded as interference fit, and its equivalent interference is set as δ_k, and a uniform pressure P_k is formed at the interface, under which a uniform contact pressure Q_k is generated at the boundary between metal shaft core and carbon fiber at the hub of flywheel. Based on the above idea, the radial and axial stresses and radial displacements of the k-th layer of the composite material can be deduced as follows in the same way.

$$\sigma_{rk}=-\frac{P_{out}^{k}}{1-\left(\frac{R_{k\min}}{R_{k\max}}\right)^{2\lambda}}\cdot\left[\left(\frac{r_k}{R_{k\max}}\right)^{\lambda-1}-\left(\frac{R_{k\min}}{R_{k\max}}\right)^{2\lambda}\cdot\left(\frac{r_k}{R_{k\max}}\right)^{-\lambda-1}\right] \tag{20}$$

$$\sigma_{\theta k}=-\frac{\lambda P_{out}^{k}}{1-\left(\frac{R_{k\min}}{R_{k\max}}\right)^{2\lambda}}\cdot\left[\left(\frac{r_k}{R_{k\max}}\right)^{\lambda-1}-\left(\frac{R_{k\min}}{R_{k\max}}\right)^{2\lambda}\cdot\left(\frac{r_k}{R_{k\max}}\right)^{-\lambda-1}\right] \tag{21}$$

$$u_{rk}=\frac{R_{(k-1)\max}}{E_\theta(1-\beta_k^{'2\lambda})}\cdot\left\{2\lambda\beta_k^{'\lambda+1}\cdot Q_k-[\lambda-v_{\theta r}+(\lambda+v_{\theta r})\beta_k^{'2\lambda}]\cdot P_k\right\} \tag{22}$$

When the k-th layer carbon fiber layer of the carbon fiber flywheel rotor is wound, the outer diameter of the composite shaft core is as follows:

$$R_{k\max}=(R_{(k-1)\max}-\delta_k+t)+\frac{R_{(k-1)\max}-\delta_k+t}{E_\theta}\cdot\frac{2\beta_k^{\lambda+1}}{1-\beta_k^{2\lambda}}\cdot\lambda\cdot P_k \tag{23}$$

When the n-th layer is wound, the shaft core formed by the former n-1 layer can be regarded as a flywheel with prestress of 0. Therefore, the radial and axial stresses of the n-th layer are as follows:

$$\sigma_{rn}=\frac{P_{\text{in}}^{n}\left(\frac{R_{n\min}}{R_{n\max}}\right)^{\lambda+1}}{1-\left(\frac{R_{n\min}}{R_{n\max}}\right)^{2\lambda}}\left[\left(\frac{r_n}{R_{n\max}}\right)^{\lambda-1}-\left(\frac{r_n}{R_{n\max}}\right)^{-\lambda-1}\right] \tag{24}$$

$$\sigma_{\theta n}=\frac{\lambda P_{\text{in}}^{n}\left(\frac{R_{n\min}}{R_{1\max}}\right)^{\lambda+1}}{1-\left(\frac{R_{n\min}}{R_{n\max}}\right)^{2\lambda}}\left[\left(\frac{r_n}{R_{n\max}}\right)^{\lambda-1}+\left(\frac{r_n}{R_{n\max}}\right)^{-\lambda-1}\right] \tag{25}$$

According to the superposition theory of plane stress, when the n-th layer winding is completed, the radial and axial stress distribution of i-th layer are as follows:

$$\sigma_{ri}=\sum_{j=i}^{n}\sigma_{ri}^{(j)},1\le i\le n \tag{26}$$

$$\sigma_{\theta i}=\sum_{j=i}^{n}\sigma_{\theta i}^{(j)},1\le i\le n \tag{27}$$

B. Structural stress and modal analysis of composite flywheel

(1) Flywheel stress analysis

Anisotropic materials have different physical properties in different directions, and the stiffness matrix of axisymmetric model in cylindrical coordinate system is:

$$\left[D_{R-Z-\theta}\right]^{-1}=\begin{pmatrix}\frac{1}{E_R} & -\frac{v_{RZ}}{E_R} & -\frac{v_{R\theta}}{E_R}\\ -\frac{v_{ZR}}{E_Z} & \frac{1}{E_Z} & -\frac{v_{\theta Z}}{E_Z}\\ -\frac{v_{\theta R}}{E_\theta} & -\frac{v_{Z\theta}}{E_\theta} & \frac{1}{E_\theta}\end{pmatrix} \tag{28}$$

Where, $\left[D_{R-Z-\theta}\right]^{-1}$ is the stiffness matrix of cylindrical coordinate system,v_{RZ}, v_{ZR}, $v_{\theta Z}$, $v_{Z\theta}$, $v_{\theta R}$ and $v_{R\theta}$ are Poisson's Ratio in different directions.

Fig. 3 shows the equivalent stress analysis when the flywheel speed is 20000 rpm. The maximum equivalent stress of the flywheel is 187.39 MPa, which appears at the contact point between the inner diameter of the wheel hub and the wheel hub disk, here is 7075 aluminum alloy material, and the allowable stress of this material can fully meet the maximum stress of the flywheel at the highest speed. At the contact between the wheel hub disc and the outer edge of the wheel hub, the equivalent stress at the contact between the outer edge of the wheel hub and the rotor is 124.97 MPa to 166.58 MPa, and the equivalent stress is also below the allowable strength of the material.

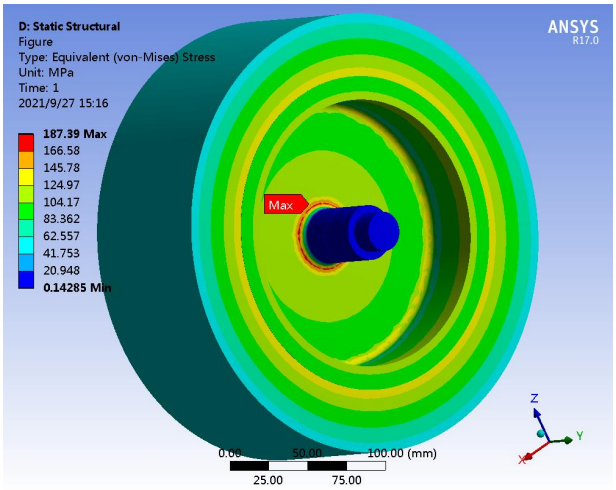

Fig. 3 Analysis of flywheel stress

The flywheel rotor is made of carbon fiber T700, which is a variety of anisotropic materials. The allowable stress of carbon fiber T700 in the longitudinal direction is large, 4200 MPa, but its allowable stress in the radial direction is very small, only 45 MPa. Compared with the allowable stress in the longitudinal direction, the allowable stress in the radial direction is much smaller than that in the longitudinal direction. Therefore, in order to prevent the radial stress of the composite flywheel rotor from exceeding the allowable stress during the high-speed rotation of the flywheel, it is very necessary to analyze the radial stress of the rotor.

As shown in Fig. 4 (a), the flywheel rotor is made of various anisotropic materials, so the Y coordinate is set as the cylindrical coordinate. In the change from the center to the edge of the flywheel, the maximum radial equivalent stress of the flywheel is 123.25 MPa. As shown in Fig. 4 (b), 100 mm to 140 mm are flywheel rotors made of carbon fiber materials. The contact position between the outer edge of the flywheel hub and the rotor is at the radius length of 100 mm, and the maximum equivalent stress on the rotor appears here is 17.1 MPa, which meets the radial allowable stress of carbon fiber T700 materials and the safety factor of 1/2 of the maximum allowable stress.

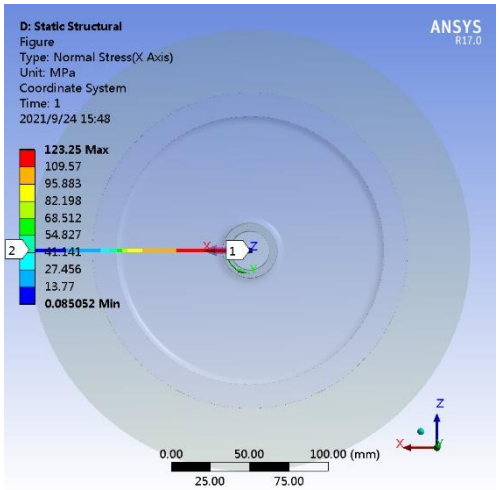

(a) Radial stress of flywheel

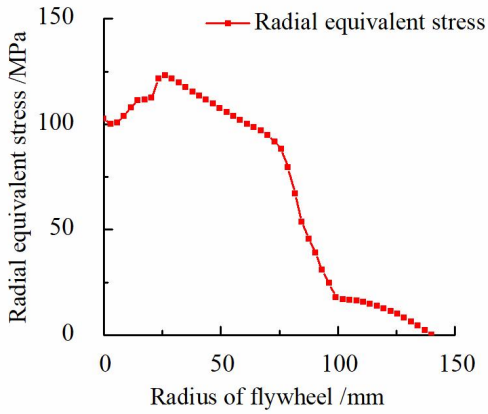

(b) Change of radial stress of flywheel

Fig. 4 Analysis of radial stress of flywheel

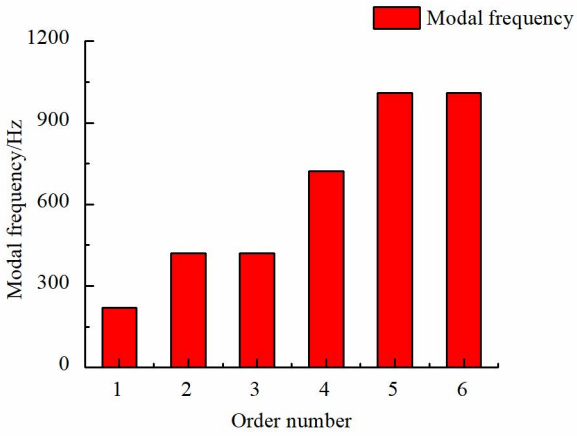

Fig. 5 The 1th-6th order modal frequency of the flywheel

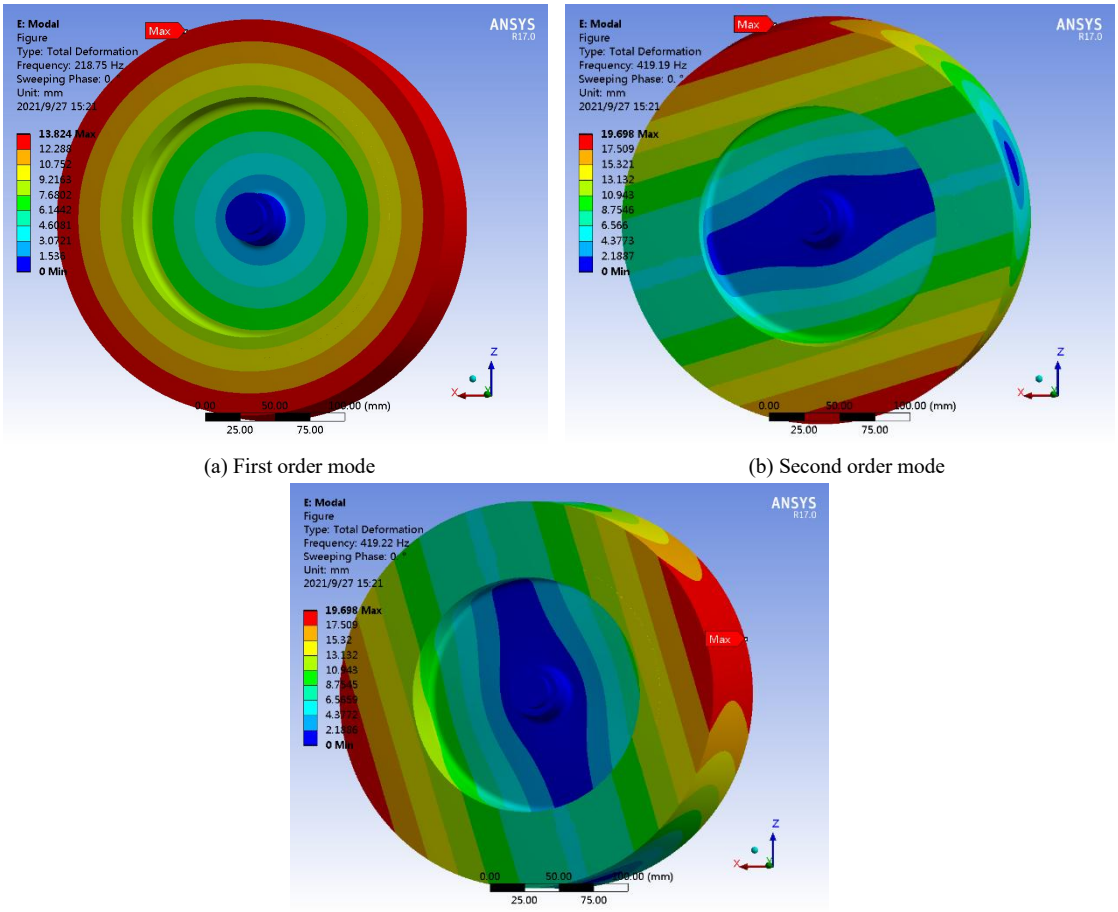

(a) First order mode

(b) Second order mode

(c) Third order mode

Fig. 6 The first three modes of the flywheel

(2) Modal analysis

The first six modes of the flywheel are shown in Fig. 5. Among them, the first-order natural frequency is 218.75 Hz, the second-order natural frequency is 419.19 Hz, the third-order natural frequency is 419.22 Hz, the fourth-order natural frequency is 721.2 Hz, the fifth-order natural frequency is 1008.5 Hz, and the sixth-order natural frequency is 1008.7 Hz. It can be seen from the figure that the natural frequencies of the second-order mode and the third-order mode, the fifth-order mode and the sixth-order mode are very close, and the natural frequencies of the two groups of modes appear in pairs.

On the premise that the maximum speed of the flywheel is 20000 rpm, the natural frequency that may affect the flywheel structure is the first three modes, and the critical speed corresponding to the natural frequency of the subsequent modes is much higher than the maximum speed of the flywheel. For example, if the natural frequency of the fourth mode is 721.2 Hz, the corresponding critical speed of the flywheel exceeds 40000 rpm, so the natural frequency of the fourth mode and after will not affect the normal operation of the flywheel. Therefore, this paper mainly analyzes the vibration modes of the first three modes.

As shown in Fig. 6 (a), from the first-order vibration mode diagram, the flywheel is mainly the vibration mode of radial tension. The position of the flywheel shaft is dark blue, indicating that its amplitude is the lowest. The color from the middle to the edge of the flywheel gradually changes from blue to red, indicating that the amplitude increases gradually with the change of position. When the speed of the flywheel reaches the first critical speed, resonance is easy to occur, and the more likely damage is located at the outer edge of the flywheel rotor. As shown in Fig. 6 (b), the vibration mode of the second-order mode of the flywheel is shown. From the figure, it can be seen that the amplitude of the flywheel is the smallest on the horizontal line passing through the center of the flywheel. In the direction along the z-axis, the amplitude increases outward layer by layer symmetrically in a ladder shape, and reaches the maximum at the edge of the carbon fiber rotor.

The second-order and third-order modal frequencies of flywheel are 419.19 Hz and 419.22 Hz respectively. The natural frequencies are very close. And the vibration modes are close, which meets the law of vibration modes appear in pairs. From the aspect of vibration modes, the two vibration modes are also very close, which is consistent with the law of vibration mode appearing in pairs. The vibration modes of the two include tension and torsion. Resonance may occur when the flywheel reaches the second-order and third-order critical speed, and the amplitude of the flywheel shaft is the smallest. Therefore, as long as the installation position of the two mechanical bearings on the flywheel shaft is correct, and the bearings provide fixation and support for the flywheel, the flywheel shaft can still work stably when resonance occurs when the flywheel reaches the critical speed. However, the flywheel hub and rotor twist along the axial direction of the flywheel, and the amplitude of the outer edge of the rotor is the largest, which may be damaged during resonance.

Due to the gyroscopic effect, the characteristic frequencies of a rotating structure are related to the speed at which it rotates. Calculating the frequencies at different

rotational speeds gives a curve of the variation of the frequency of each mode with speed, called a Campbell diagram. From the flywheel Campbell diagram Fig. 7, it can be seen that the gyroscopic effect of the flywheel has a clear influence on the modes. As the speed increases, the frequency curve may be shifted to cross the frequency curve of another mode, the frequency curve of a second order mode shifted downwards to intersect the frequency curve of a first order mode, and the frequency curve of a third order mode shifted upwards to cross the frequency curve of a fourth order mode. The black line shows the set flywheel speed up to 2094 rad/s, the intersection of which with the frequency curve of each mode is the critical speed. As can be seen from the graph, the critical speed of this flywheel is 1374.5 rad/s for the first order and 1581.9 rad/s for the second order, while the intrinsic frequency curve no longer intersects the speed curve above the third order.

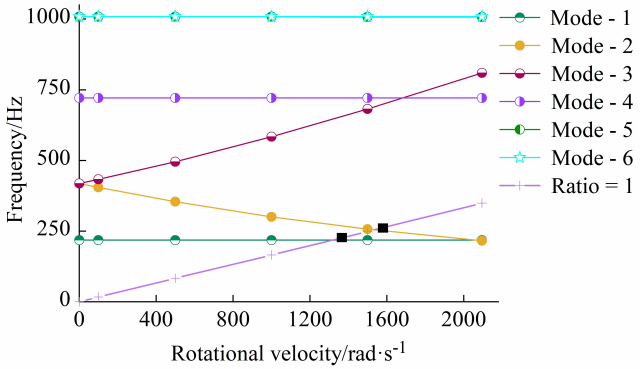

Fig. 7 Campbell diagram

IV. Analysis of the Efficiency Characteristics of Electromechanical Flywheel

A. Electromechanical flywheel loss analysis and modelling

The losses in the operation of the electromechanical flywheel unit mainly include wind resistance losses of the flywheel rotor, bearing losses, mechanical drive friction losses and motor losses. Among them, the mechanical drive friction loss is taken as a constant value in this paper, and the motor loss is determined by the calculation of the motor efficiency Map diagram provided by the manufacturer. The wind resistance loss of the flywheel rotor is divided into two parts: the friction loss between the outer wall of the rotor and the air and the friction loss between the end face of the rotor and the air.

The wind resistance loss of the flywheel rotor is divided into two parts: the friction loss between the outer wall of the rotor and the air and the friction loss between the end face of the rotor and the air, where the friction loss power P_1 between the outer wall of the rotor and the air can be calculated by the following formula.

$$P_1 = 2\pi R_{fw} h\mu \frac{R_{fw}^2 \omega^2 \left(1+\delta / R_{fw}\right)^2}{\delta\left(1+\delta / 2R_{fw}\right)} \times \frac{1}{1+2AK\left(\delta / R_{fw} + 1/\left(1+\delta / R_{fw}\right)\right)} \tag{29}$$

Where, R_{fw} is the rotor radius, h is the rotor height, μ is the internal friction factor of the gas, δ is the rotor to outer wall clearance, A is the sliding coefficient, and K is the Knudsen number.

$$P_2 = \frac{\pi}{2} R_{fw}^4 \mu\omega^2 \left[\frac{1}{\delta_d\left(1+2AK\right)} + \frac{1}{\delta_u\left(1+2AK\right)}\right] \tag{30}$$

Where, δ_d is the upper face to sleeve clearance, δ_u is the lower face to sleeve clearance.

During the high-speed rotation of the flywheel, friction loss will be generated at the bearing, and its wear rate is taken as 0.01, then the bearing loss power can be calculated by the following formula.

$$P_b = 0.01 P_{fw} \tag{31}$$

Where, P_b is the bearing loss power; P_{fw} is the flywheel power.

B. Analysis of the efficiency characteristics of electromecha -nical flywheel

The electromechanical flywheel efficiency analysis is carried out in the deceleration a mode as an example. When the electromechanical flywheel is operating in deceleration a mode, both the governor motor and flywheel are involved in braking, the governor motor generates electricity, the flywheel speed increases and the vehicle speed decreases. The kinetic energy of the vehicle is partly transformed into kinetic energy of the flywheel, while partly transformed into electrical energy by the governor motor and stored in the lithium battery. At this point, the working power of the electromechanical flywheel system needs to be considered when the flywheel is at different state of energy (SOE). From the above system loss analysis, the electromechanical flywheel working efficiency in this mode can be deduced.

$$\eta_{sys} = \frac{P_{fw} + P_e}{P_{dw}} = \frac{P_{fw} + P_{srm}/\eta_{srm}}{\left(P_e + P_{fw} + P_{cw} + P_b\right)/\eta_T} \tag{32}$$

Where, η_{sys} is the efficiency of the electromechanical flywheel system, P_e is the battery output, P_{fw} is the flywheel power, P_b is the flywheel bearing wear power, P_{cw} is the flywheel wind resistance power, η_{srm} is the motor efficiency and η_T is the mechanical efficiency of the drivetrain.

As shown in Fig. 8, the calculations determine the electromechanical flywheel system efficiency for different flywheel SOE states. Overall, the electromechanical flywheel efficiency range is 0.76-0.87. In addition, the efficiency of the electromechanical flywheel system is generally in a decreasing trend as the flywheel SOE increases. The main reason for this is that as the SOE increases, the increase in flywheel speed will inevitably cause an increase in wind resistance losses, bearing losses and mechanical drive friction losses of the device. The efficiency characteristics of electromechanical flywheel operation in starting and acceleration modes are not detailed in this paper.

V. Analysis of Vehicle Dynamics and Economy

A. Dynamics analysis

As shown in Fig. 9, the original vehicle uses a single-motor front axle direct drive solution. Compared with this solution, the electromechanical flywheel device can significantly increase the peak drive torque of the vehicle powertrain when the vehicle is involved in hill climbing dri-

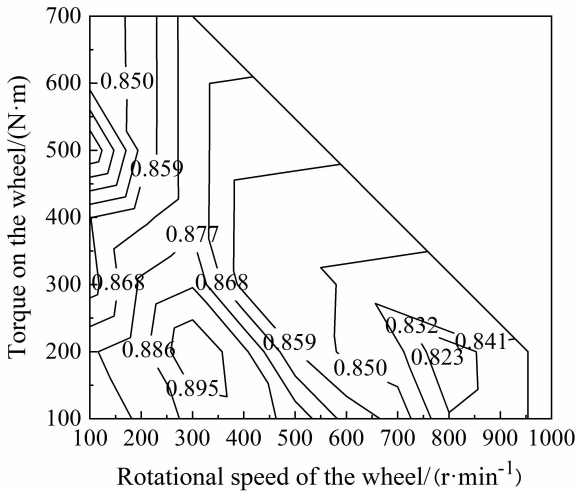

(a) SOE=0.1

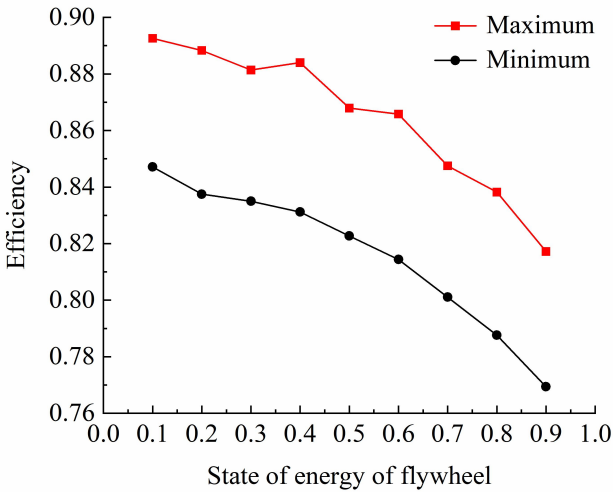

(b) 0.1≤SOE≤0.9

Fig. 8 Efficiency characteristics of electromechanical flywheel in reduction a mode

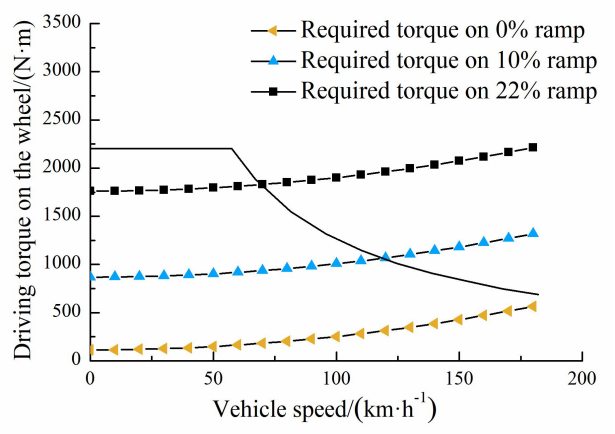

(a) Original scheme of single motor drive

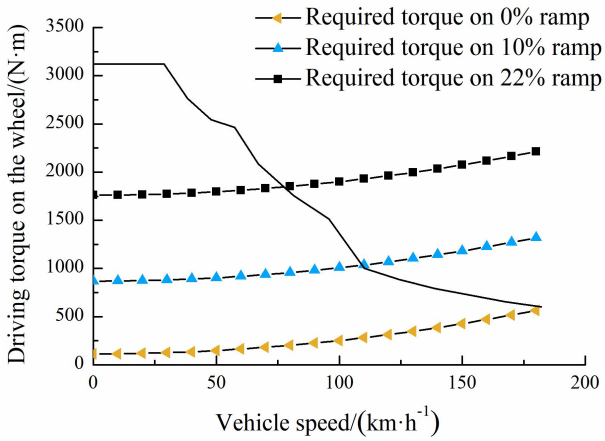

(b) New scheme of electromechanical flywheel hybrid

Fig. 9 Comparison of the climbing performance

ve, improving the vehicle's hill climbing performance and increasing the maximum hill climbing degree of the vehicle by 23.2 %.

B. Economic analysis

As shown in Fig. 10, in the J1015 operating conditions, the original single-motor direct drive solution is limited by the single-stage variable speed topology, and the single motor will inevitably operate in the inefficient operating conditions A1 and A2 (low to medium speed, high load operating conditions) at some point in time, resulting in low overall vehicle operating efficiency. With the intervention of the electromechanical flywheel device, the efficiency of the main drive motor can be optimised by shifting the operating points in the former inefficient operating domain A1 and A2 to the efficient operating domain B1 and B2 of the main drive motor, which increases the average efficiency of the main drive motor by 8.3 %.

Under J1015, the proportion of the electromechanical flywheel hybrid powertrain operating at high efficiency (>90 % efficiency) is 41.6 %, an increase of 19.9 % compared to the original single-motor direct-drive solution, while the proportion of operating at low efficiency (< 80% efficiency) is 11.1 %, a reduction of 13 % compared to the original single-motor direct-drive solution. Overall, the average efficiency of the entire vehicle powertrain cycle under J1015 conditions has increased by 8.2 %.

As shown in Fig. 11, the power variation characteristics of the auxiliary battery flywheel and the main energy source lithium battery under J1015 operating conditions are given for the two solutions. Compared with the single energy source of the original vehicle, the intervention of the electromechanical flywheel battery, with the advantage of the flywheel's instantaneous high power absorption or output power, can effectively slow down the power fluctuation of the main energy source, reduce the instantaneous peak power impact on the efficiency of the lithium battery, and achieve the effect of cutting the peak and compensating the valley. Compared with the original single energy source solution, thanks to the electromechanical flywheel battery, the operating current range of the lithium battery is reduced to -60 A to 60 A, a reduction of 53.8 %; the efficiency range is increased to 0.85-0.94, and the cycle efficiency is increased by 6.7 %, respectively.

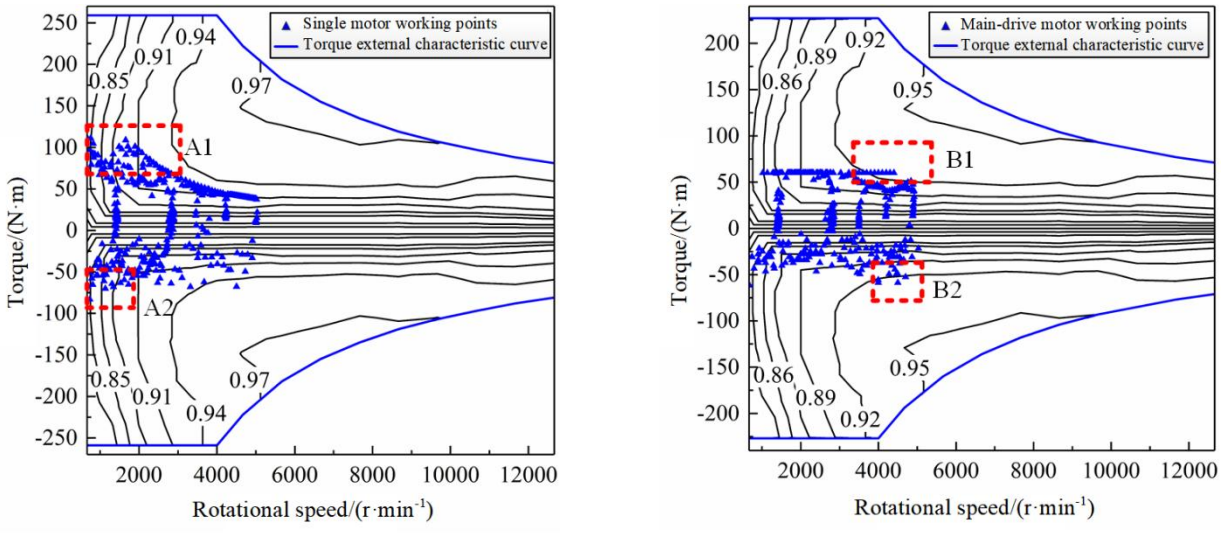

(a) Motor efficiency distribution of the original scheme

(b) Motor efficiency distribution of the new scheme

Fig. 10 Distribution of motor efficiency under J1015 cycle

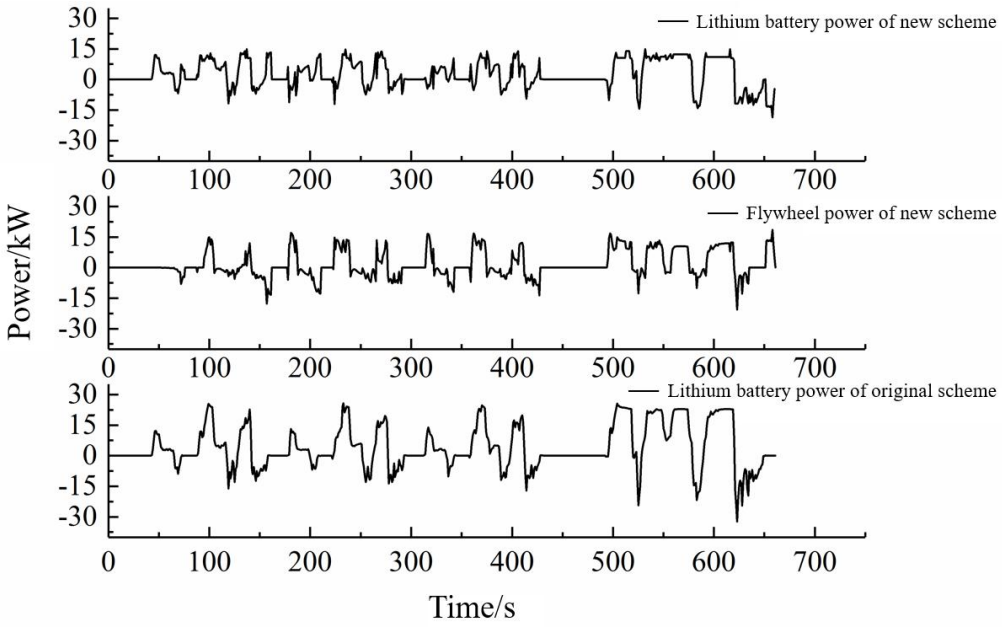

Fig. 11 Power characteristics of flywheel and lithium battery under J1015 cycle

VI. Conclusion

(1) According to the research, when the flywheel speed is 20000 rpm, the maximum equivalent stress of the flywheel is 187.39 MPa, which is less than the allowable stress of 7075 aluminum alloy. The equivalent stress at the contact between the outer edge of the wheel hub and the rotor is 124.97 MPa to 166.58 MPa, which is also lower the the allowable strength of material. The radius of the contact position between the outer edge of the flywheel hub and the rotor is 100 mm, and the maximum equivalent stress on the rotor is 17.1 MPa. This value meets the radial allowable stress of carbon fiber T700 material, and the safety factor of 1 / 2 of the maximum allowable stress.

(2) The loss of electromechanical flywheel hybrid device mainly includes the wind resistance loss of flywheel rotor, bearing loss, mechanical transmission friction loss and motor loss. The loss of the device is affected by the SOE of the flywheel.With the increase of SOE, the increase of flywheel speed will lead to the increase of wind resistance loss, bearing loss and mechanical driving friction loss of the device, and then the efficiency of the electromechanical flywheel system is reduced.

(3) Compared with the original single motor drive scheme, the maximum climbing angle of the vehicle is increased by 23.2%. The average operating efficiency under J1015 cycle condition is increased by 8.2% due to the improvement of vehicle power transmission system efficiency.

References

[1] Strategy advisory committee on energy-saving and new energy vehicle technology roadmap, Chinese Society of Automotive Engineering, “Energy-Saving and New Energy Vehicle Technology Roadmap,” Beijing: Machinery Industry Press, 2016.

[2] B. Sun, S. Gao, C. Ma, “System Power Loss Optimization of Electric Vehicle Driven by Front and Rear Induction Motors,” International Journal of Automotive Technology, vol. 19, no.1, pp121-134, 2018.

[3] Lei Zhang, Xiao Song Hu, Zhen Po Wang, “Review on supercapacitor Management Technology and Its Application in Electric Vehicles,” Chinese Journal of Mechanical Engineering, vol. 53, no.16, pp32-43+69, 2017.

[4] Chung Neng Huang, Yui Sung Chen, "Design of magnetic flywheel control for performance improvement of fuel cells used in vehicles," Energy, vol. 118, pp840-852, 2017.
[5] A. Dhand, K. Pullen, "Review of flywheel based internal combustion engine hybrid vehicles," International Journal of Automotive Technology, vol. 14, no.5, pp797-804, 2013.
[6] A. Dhand, K. Pullen, "Review of Battery Electric Vehicle Propulsion Systems Incorporating Flywheel Energy Storge," International Journal of Automotive Technology, vol. 16, no.3, pp487-500, 2015.
[7] J. G. R. Hansen, D. U. O' Kain, "An Assessment of Flywheel High Power Energy Storage Technology for Hybrid Vehicles," Oak Ridge National Laboratory, 2011.
[8] A.A. Khodadoost Arani, H. Karami, G.B. Gharehpetian, et al., "Review of flywheel energy storage systems structures and applications in power systems and microgrids," Renewable and Sustainable Energy Reviews, vol. 69, pp9-18, 2017.
[9] F. Bottiglione, G. Carbone, L.D. Novellis, et al., "Mechanical hybrid KERS based on toroidal traction drives: an example of smart tribological design to improve terrestrial vehicle performance," Advances in Tribology, pp1-9, 2013.
[10] A. Dhand, K. Pullen, "Optimal energy management for a flywheel assisted battery electric vehicle," Proceedings of the Institution of Mechanical Engineers Part D Journal of Automobile Engineering, vol. 229, no.12, pp1672-1682, 2015.
[11] Binbin Sun, Tianqi Gu, Pengwei Wang, et al., "Optimization Design of Powertrain Parameters for Electromechanical Flywheel Hybrid Electric Vehicle," IAENG International Journal of Applied Mathematics, vol. 52, no.2, pp450-457, 2022.